



HAL
open science

Hybrid numerical method for the ultrasonic wave propagation velocity in orthotropic materials

Xi Zhang, Frédéric Dubois, Nicolas Sauvat, Mokhfi Takarli

► **To cite this version:**

Xi Zhang, Frédéric Dubois, Nicolas Sauvat, Mokhfi Takarli. Hybrid numerical method for the ultrasonic wave propagation velocity in orthotropic materials. *Wood Science and Technology*, 2022, 56 (6), pp.1605-1630. 10.1007/s00226-022-01416-8 . hal-04086310

HAL Id: hal-04086310

<https://unilim.hal.science/hal-04086310>

Submitted on 10 May 2023

HAL is a multi-disciplinary open access archive for the deposit and dissemination of scientific research documents, whether they are published or not. The documents may come from teaching and research institutions in France or abroad, or from public or private research centers.

L'archive ouverte pluridisciplinaire **HAL**, est destinée au dépôt et à la diffusion de documents scientifiques de niveau recherche, publiés ou non, émanant des établissements d'enseignement et de recherche français ou étrangers, des laboratoires publics ou privés.

Hybrid Numerical Method for the Ultrasonic Wave Propagation Velocity in Orthotropic Materials

Xi Zhang ^(1, 2), Frédéric Dubois ⁽¹⁾, Nicolas Sauvat ⁽¹⁾, Mokhfi Takarli ⁽¹⁾

(1) Université de Limoges, Laboratoire de Génie Civil, Diagnostic et Durabilité, GC2D – EA 3178, Boulevard Jacques Derche, 19300-Egletons, France

(2) China Aerospace Academy of Architectural Design&Research Co.,Ltd, China

Scientific Contact: Prof. Frédéric Dubois, frederic.dubois@unilim.fr

Abstract

This paper deals with a new hybrid method coupling an analytical and finite element approach for the calculation of the ultrasonic wave propagation velocity in orthotropic materials applied to timber elements. First, the method consists of integrating an analytical model described for orthotropic materials by considering a misalignment of the ultrasonic wave propagation direction with the main orthotropic reference. A second step calls for implementation in a finite element approach. This coupling allows for the computation of wave propagation velocity by assuming a heterogeneous material induced by means of a moisture content gradient in timber elements exposed to outdoor conditions inducing a non-homogeneous distribution of mechanical properties such as moduli of elasticity integrating the orthotropic character of wood. The result of this work proposes a highly efficient hybrid numerical approach, yet without solving the dynamic finite element problem, which typically requires a very long computation time while benefiting from a finite element support to project the different mechanical and hydric fields.

Keywords: ultrasonic techniques, orthotropic material, timber elements, finite element method, hybrid method, heat and mass transfer.

Acknowledgements

This work is part of the research project 'SOUBOIS' founded by the French region 'Nouvelle Aquitaine'.

1. Introduction

In the context of maintenance, repair or reinforcement and requalification of timber structures, engineers need to assess the load-bearing element residual strength. For this purpose, several strategies are employed, such as monitoring techniques and visual inspections leading to a structural diagnosis and

structure recalculation. At the present time, non-destructive testing (NDT) techniques are widespread (Vössing and Niederleithinger 2018). It is now recognized that the structural strength of wooden elements is strongly correlated with both their density and elastic properties. For example, in the case of mechanical grading of timber for the glulam industry, several control strategies are employed. Although static bending tests are still used today, NDT methods offering faster implementation are increasingly being developed. Moreover, these techniques can be used *in situ*, yet only the longitudinal modulus of elasticity is characterized. As such, ultrasonic methods allow obtaining other elasticity properties, which proves to be important in the case of wood materials.

Timber elements are characterized by a cylindrical orthotropy and a material heterogeneity induced by the wood anatomy and moisture content gradients during the drying and rewetting phases under outdoor climate conditions. They have unique and independent mechanical properties in the three principal directions: longitudinal, radial, and tangential. As an orthotropic material, wood is defined by ten independent constants that describe its elastic behavior: density, three moduli of elasticity (MOE), three moduli of rigidity (G), and three independent Poisson's ratios (ν). Typically, these elastic parameters are determined by static testing, which involves the destructive testing of a centimetric-scale specimen, and involve mechanical testing methods, such as four-point bending compression and tensile tests. Thus, the use of Non-Destructive Testing (NDT) instead of static destructive testing is an attractive alternative.

NDT systems have long been used to assess the physical, mechanical or chemical properties of materials and structures in determining changes in shape, deformations, stresses or even humidity or any other pollutant. The principle behind NDT is to perform measurements while minimizing their impacts on the measured properties as well as on the integrity of the element under study. With several years of hindsight, (Bucur 2006; Kollmann et al. 2012; Norimoto and Yamada 1970; Ross 1994; Torgovnikov 1993), NDT technologies applied to wood rely on transverse measurement techniques. which can be associated with inverse methods using complementary parallel modeling. Let's cite as an example the image analysis method like correlation or tracking markers (Silva et al., 2022) and resistive measurements (Nguyen et al., 2017), dielectric or electromagnetic methods (Matsunaga et al., 2022), which are more sensitive to humidity.

Part of the present study also focuses on ultrasound techniques. Several authors have used the velocity of ultrasonic waves to diagnose and monitor cracks as well as to evaluate the elastic properties in civil engineering structures, whether concrete or wood (Alves et al. 2015; Cuxac, 1991). Many references are available on perfect samples (Bucur 2006; Kabir et al. 1998; Kabir 2001; Wang, 2008; Espinosa et al., 2018). However, measurements on timber are rare, and the issue of moisture heterogeneity, to the authors' knowledge, has never been addressed. In the context of characterizing elasticity properties, measurement by means of ultrasound wave propagation represents a commonly used method today for controlling timber elements in order to determine the resistance class in new elements or the level of residual strength in older elements. Yet such a measurement is often limited to the characterization of the longitudinal modulus of elasticity. Should this property be considered as sufficient to deduce an equivalent resistance, then ultrasonic analysis techniques are indeed sensitive to all elastic parameters composing the stiffness tensor. On the other hand, this step requires developing an identification strategy based on the constitutive equations of the wave propagation process in an orthotropic and heterogeneous medium.

Ultrasonic waves are mechanical vibrations, with a frequency greater than 20 kHz. As disturbances of a deformable medium, they propagate in all elastic media, whether solid, liquid or gaseous. The ultrasonic wave experiences several disturbances, for example reflection, refraction, diffusion and absorption. In the past, ultrasonic methods had already been studied for wood materials (Sakai et al., 1990). The variations in characteristic quantities (such as the velocity or attenuation factor) of the propagation of ultrasonic waves depend on mechanical properties (density, elasticity). The typical frequency range of 20 kHz to 200 kHz is suitable for high-energy attenuation (McDonald et al. 2014; Zisi and Dix 2017).

Depending on the material anisotropy, the compression wave propagates at different velocities as a function of the angle between the longitudinal direction and the propagation direction (i.e. fiber angle). In a wood material, the compression wave velocity in the longitudinal direction is higher by 5000 to 6000 m.s⁻¹. In contrast, in both the radial and tangential directions, the compression wave velocity equals about 20% to 30% of the longitudinal direction velocity, i.e. 1000 to 2000 m.s⁻¹ (Masumi et al., 2011). The propagation rates depend on the wood species, density, and the moisture content distribution.

Moreover, the ultrasonic wave velocity is sensitive to moisture content and its distribution (De Oliveira et al., 2005; Gonçalves et al. 2018; Dündar et al. 2016).

This work is based on an experimental protocol involving a Douglas fir glulam beam exposed to ambient humidity variations that produce a hydric gradient, in turn inducing heterogeneity in mechanical properties. This protocol is presented in the first part, including experimental ultrasonic wave velocity measurements. An analysis of the experimental propagation velocities relies on the use of a numerical model in the aim of ultimately deducing the spatial distribution of both the elastic properties and moisture content fields. In this case, this paper deals with an approach which a correlation between propagation wave velocities and elastic properties by considering orthotropy and their heterogeneities induced by the moisture content distribution. Because inverse methods could integrate this tool, it must be fast and compatible with a spatial representation of mechanical properties.

In this context, numerical methods using finite elements or finite differences make it possible to model the process of propagation of ultrasonic waves in heterogeneous anisotropic media, and for complex geometries, they have the disadvantage of mobilizing a strong computer resource inducing long resolution times. This drawback does not allow these numerical methods to be used in inverse method or optimization algorithms. Other methods like spectral methods can be an alternative but still present non-instantaneous resolution times (Sridhar et al., 2006; Komatitsch et al. 2000; Rosenkrantz et al. 2019).

Beforehand however, it is necessary to develop an efficient and fast numerical model for implementation in an inverse analysis loop. Some works are based on analytical models that can integrate material orthotropy but are limited to simple geometries (Zhang et al., 2021). Other analytical approaches allow the reconstruction of the stiffness tensor in orthotropic or viscoelastic materials but require a dynamic loading in the main orthotropic referential (Orta et al., 2021).

Thus, the authors propose a new hybrid method coupling the efficient of an analytic formalism and its finite element implementation coupling calculation speeds given by an analytical model and the

considering of heterogeneities (moisture content distribution or elastic property heterogeneities) allowed by the numerical finite element method.

Prior to presenting the development of this analytical model, the second section lays out the standard resolution approach using both the finite element method and an incremental time resolution that includes the orthotropic properties characterizing wood materials. Unfortunately, while this model does deliver a high calculation accuracy, it nonetheless requires a powerful spatial and temporal discretization, thus inducing excessively long calculation times.

To address the computational cost issue, a third section discusses the development of an analytical model that includes both the orthotropic characteristics of the material and the orientation of the wave propagation path within the main orthotropic reference frame. To simplify analytical developments, only the 2D approach will be presented by choosing the RL plane. For homogeneous water content conditions, this model is numerically validated by comparing its results with experimental data and the standard finite element model.

Since this analytical model is only compatible with a homogeneous medium, herein a hybrid approach is proposed combining the advantages of a fast analytical model with a finite element discretization to allow considering a mechanical or moisture heterogeneity. Lastly, an application is shown using experimental results under heterogeneous water content conditions and the standard dynamic finite element resolution.

2. Experimental set-up

Wood sample

The main interest of this work lies in the determination of wood mechanical properties by studying the effects of both the fiber angle and geometry on the wave propagation velocity on glulam beams. The ultrasonic measurements were carried out on a Douglas fir glulam measuring 3800 mm long by 80 mm thick by 280 mm wide, with each lamella being 40 mm wide. The moisture content of the sample was homogeneous and equal to 11.9%.

Instruments and method for Time-of-Flight (TOF) detection

The ultrasonic device (Pundit PL-200 developed by Proceq, Switzerland) was used to determine the TOF (Time of Flight) of the stress wave (Fig. 1); it includes a pulse generator with a tension range between 50 V and 400 V, and a reception gain factor extending from 0 to 80dB. The time resolution was 0.1 μs and the voltage was measured at $\pm 30.52 \mu\text{s}$ on a 16-bit scale. For the structural scale beam tests, a pair of piezoelectric transducers was used to excite compression waves (P wave) with a resonant frequency of around 54 kHz \pm 5 kHz and a diameter of 36.77 mm. Resonant-type piezoelectric transducers (transmitters and receivers) were chosen to compensate for the strong attenuation in wood. Ultrasonic testing couplings were needed to ensure good contact between the transducers and the material. The calculation of the time of flight requires to determine, with precision, the wave arrival time at the receiver sensor. Several criteria are presented in the literature, for example the Hinkley or sliding maximum criteria (Kurz et al. 2005; Lasaygues et al., 2014). However, from experimental campaigns applied to concrete or wood material, the Akaike criterion is usually used (Zhang 2021). Prior to taking any measurements, the instrument was calibrated with a reference plexiglass block characterized by its time of flight of 25.4 μs corresponding to a propagation velocity of 4000m.s⁻¹. The transmission time from transmitter to receptor was recorded by the ultrasonic system, and the ultrasonic velocity was calculated by dividing the distance propagation by the transmission time.

After measuring the wave propagation signal, the Akaike information criteria (AIC) picker (Zhang 2003) was used to estimate the order of autoregressive (AR) models to determine the trigger time. In this case, the signal intervals were assumed to be two time series (i.e. noise and signal), differing before and after the trigger time point (Fig. 1).

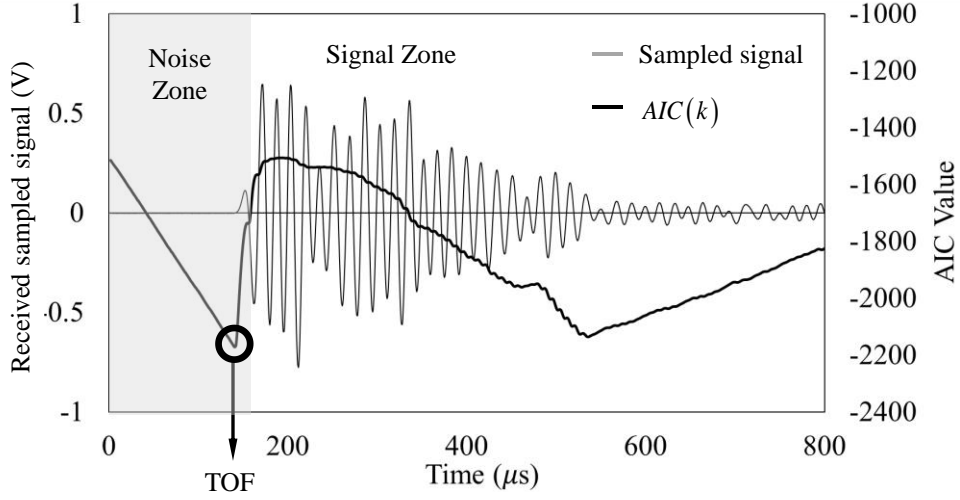


Fig. 1 TOF determination by means of the AIC method

The TOF is given by the minimum of the AIC function, as calculated on a digitized sampled signal discretized in N points (Fig. 1). Each point is referenced x_k , with k designating the range point:

$$TOF = \min_{k \in [1, \dots, N]} (AIC(k)) \quad (1)$$

The AIC function is defined below:

$$AIC(k) = k \cdot \log\left(\text{Var}\left(x_1^k\right)\right) + (N - k) \cdot \log\left(\text{Var}\left(x_{k+1}^N\right)\right) \quad (2)$$

$$\text{with: } \text{Var}\left(x_i^j\right) = \frac{1}{j} \sum_{n=i}^j \left(x_n - X_i^j\right)^2 \quad \text{and} \quad X_i^j = \frac{1}{j-i+1} \cdot \sum_{n=i}^j x_n \quad (3)$$

To study the propagation process and behavior of ultrasonic waves in the various directions from longitudinal to tangential, a series of points was plotted on the cross-section to measure the time of flight along different propagation paths in a median XY plane. The transmitter was placed on the lower beam face. Since we were interested in obtaining different polarization angles, the receptor was moved on the upper face and beam sides, as shown in Fig. 2, with an angle ranging from 0° to 180° between the longitudinal direction (L) and the radial (R) or tangential (T) directions. This angle corresponds to a misalignment of the propagation path with respect to the longitudinal direction considering a transverse isotropy in the RT plane formed by the radial and tangential directions.

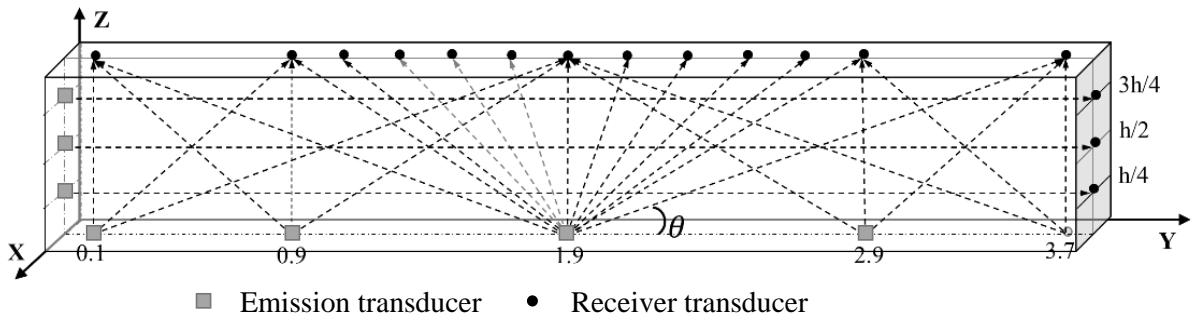


Fig. 2 Ultrasonic transducer locations for measuring wave velocity vs. angle range

By measuring the distance D between the transducers (transmitter and receiver), the angle θ between the propagation direction of the ultrasonic wave and the wood fiber direction could be defined. The ultrasonic wave propagation velocity V was calculated using the following relation:

$$V = \frac{D}{TOF} \quad (4)$$

Moisture content evolution and ultrasonic wave velocity dependence

To measure the ultrasonic wave velocities from the longitudinal to tangential directions at different moisture contents, the beams were recessed under an irrigation system for a sufficiently long period of time (Fig. 3), and then weighed and recorded. To increase the efficiency of the irrigation, the beam is covered with tarpaulins to keep a high level of humidity on its upper part. Initially, a homogeneous moisture content (at 11.9%) was considered, but after 50 rewetting days, the moisture content became heterogeneous with an average value of 17.6%.



Fig. 3 Irrigation principle

The relationship scatter diagram between θ and the ultrasonic wave velocity V_p in the various directions is plotted in Fig. 4.

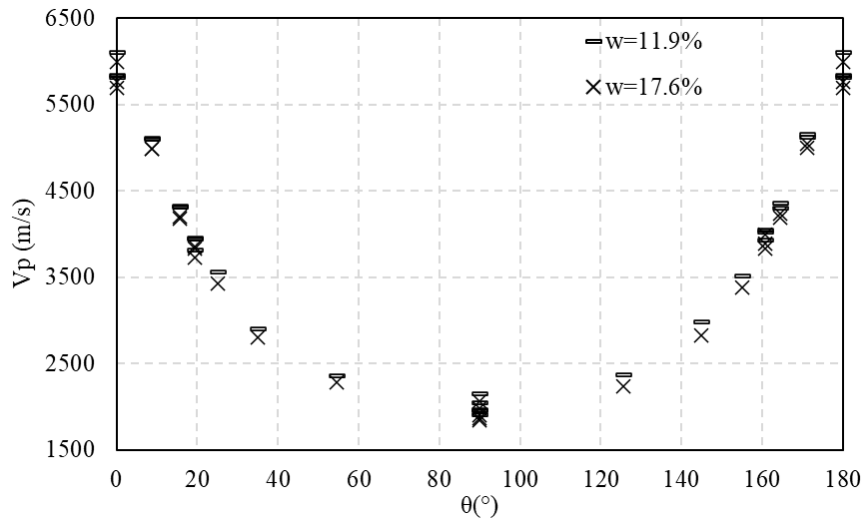


Fig. 4 Effect of grain angle on the propagation velocity of ultrasonic waves vs. moisture content

These results highlight a decrease in the ultrasonic wave velocity (between 1% and 4%) according to an increase in average moisture content being explained by a decrease in elastic modulus in the longitudinal-radial plane. However, this measurement considers an average ultrasonic wave velocity along the wave propagation path. This small difference can be attributed to the measurement uncertainty linked to the heterogeneity of the material. However, the downward trend in speeds is homogeneous with more marked drops for low speeds than for high speeds, which is explained by the fact that the longitudinal modulus of elasticity is slightly less sensitive to moisture content than radial and tangential moduli. Moreover, for an angle θ of 0° , several measurements for different propagation paths along fibers highlight this heterogeneity, whether at the scale of the material or also at the scale of the moisture field distribution. In this case, incorporating such a heterogeneity requires developing a specific finite element approach that allows describing a more realistic wave velocity distribution.

3. Finite element model for wave propagation problems

Dynamic finite element developments

An ultrasonic wave propagating in an elastic anisotropic material creates particle displacement over time, thus inducing strain and stress perturbations. The ultrasonic wave propagation in material can be

expressed via the equations of wave motion, which can be determined using a combination of Newton's second law and Hooke's law (Royer et al., 1996):

$$\rho \cdot \frac{\partial^2 u_i}{\partial t^2} = C_{ijkl} \cdot \frac{\partial^2 u_l}{\partial x_j \partial x_k} \quad (5)$$

where u_i and u_l denote the displacement components of a material point M defined by its coordinates x_j in a Cartesian reference. ρ is the material density, assumed to be homogeneous like C_{ijkl} , which represents the components of elastic stiffness tensor \mathbf{C} , in accordance with the following Hooke's law:

$$\underline{\underline{\sigma}} = \mathbf{C} \cdot \underline{\underline{\varepsilon}} \text{ or } \sigma_{ij} = C_{ijkl} \cdot \varepsilon_{kl} \text{ with } (i, j, k, l) \in \{1, 2, 3\}^4 \quad (6)$$

σ_{ij} and ε_{kl} are the components of the stress and strain tensors, $\underline{\underline{\sigma}}$ and $\underline{\underline{\varepsilon}}$, respectively.

The formulation in (5) has been integrated into an explicit numerical algorithm implemented in the finite element software Castem. Let's consider a three-dimensional discretization. As shown in Fig. 5, the emission sensor is represented as a cylindrical contact surface, on which a pulse force is imposed.

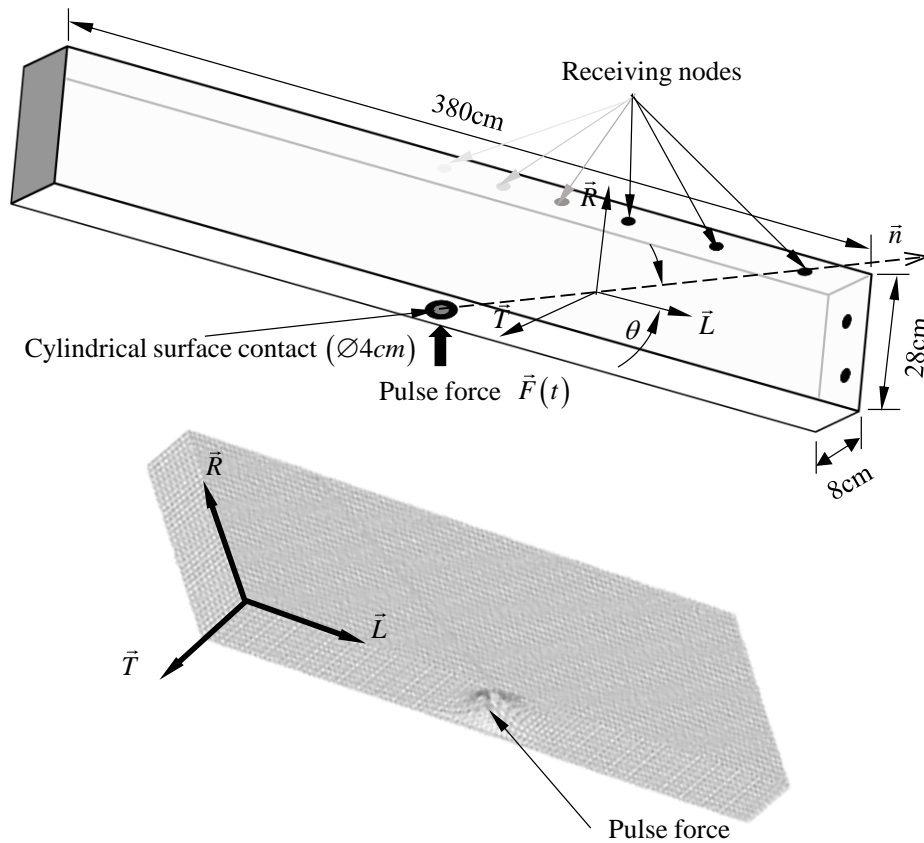


Fig. 5 Positioning of transmit and receive sensors and 3D deformed finite element mesh

The receiving sensors are placed directly on the mesh nodes where the temporal evolution of displacements is calculated. One transmitter is placed on the middle and lower beam face. All receiving sensors enable mapping the wave propagation paths, as defined by their normal \vec{n} and angle θ with the longitudinal direction.

To generate a compression wave, at the cylindrical surface contact, a pulse force is imposed defined by the following semi-sinusoidal form, Fig. 6:

$$\vec{F}(t) = \vec{F}_o \cdot \sin(2 \cdot \pi \cdot f \cdot t) \cdot H\left(t - \frac{1}{2 \cdot f}\right) \quad (7)$$

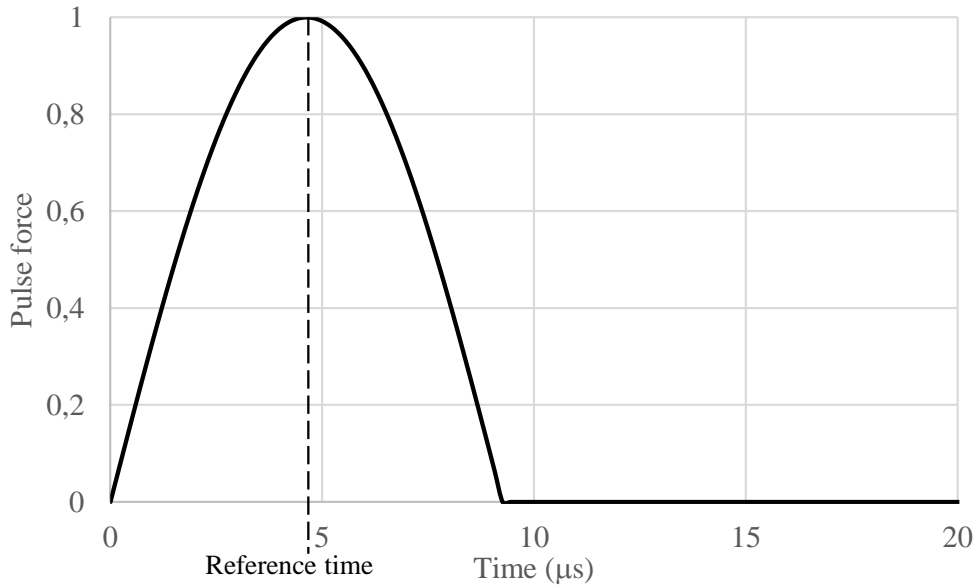


Fig. 6 Time evolution of the pulse force

\vec{F}_o is the normal force amplitude distributed at the contact surface. In accordance with a linear elastic behavior, we have opted for a unit amplitude. The frequency f is fixed at 54 kHz, as dictated by the experimental ultrasonic sensors. The Heaviside function $H(t)$ allows limiting the pulse during one half-period. The time evolution of the pulse force is displayed in Fig. 6. In this context, the reference time corresponds is calculated at the pic of the semi-sinusoidal displacement. The finite element discretization necessitates an adaptation of element size Δx with wavelength λ , such that (Pradhan 2014; Seron et al. 1990):

$$\Delta x \leq \frac{\lambda}{N} \quad (8)$$

In this study, a convergence algorithm allows setting N at 11, which corresponds to an element size of less than 2.7 mm. Similarly, the time discretization Δt is defined by its critical value as follows:

$$\Delta t \leq \frac{\Delta x}{V} \quad (9)$$

where V denotes the ultrasonic wave propagation speed. Given the speed of ultrasonic wave I in wood exceeding $1,600 \text{ m}\cdot\text{s}^{-1}$, the time discretization has been fixed at $0.48 \text{ }\mu\text{s}$. Under these conditions, the finite element mesh is presented in the form of its deformations due to the pulse force.

The finite element resolution calls for a step-by-step procedure implemented in the software Castem (explicit scheme), as adapted for a time resolution of the dynamic problem described below:

$$[M] \cdot \frac{\partial^2 \{\vec{u}\}}{\partial t^2} + [D] \cdot \frac{\partial \{\vec{u}\}}{\partial t} + [K] \cdot \{\vec{u}\} = \{\vec{F}\}_{ext} \quad (10)$$

$[M]$, $[D]$ and $[K]$ are the mass, damping and stiffness matrices, respectively. $\{\vec{u}\}$ denotes the nodal displacement vectors, and $\{\vec{F}\}_{ext}$ the external force vector. The material definition includes orthotropic properties. On the other hand, for an orthotropic medium, the software does not make it possible to adopt absorbing boundary conditions making it possible to limit the echoes at the boundaries of the geometry, which complicates the determination of the time of flight. The numerical solution provides a timetable for the displacement field. The wave propagation velocity is calculated by considering the distance between transmitter and receiver points and the Time of Flight, which is the difference in time between these two points, as calculated by studying the displacement signal shown in Fig. 7.

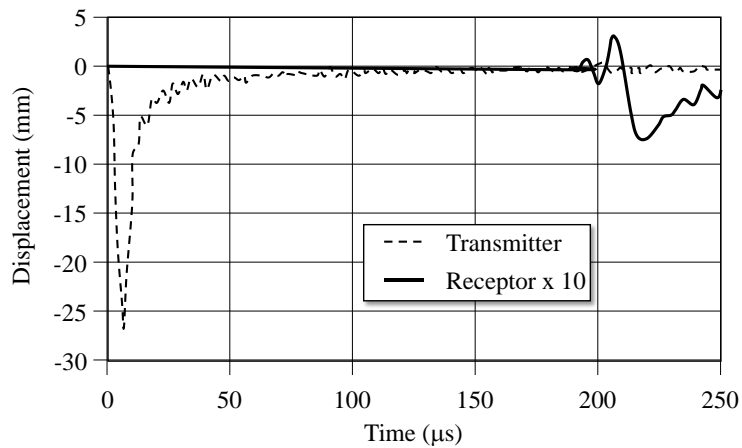


Fig. 7 Displacements for points i and j vs. time of propagation

Moreover, the mapping of elastic properties can include a moisture content-dependent term. However, computation time can be very long and must be extended should the wave not reach the reception point. This conclusion prompts us to propose an alternative approach based on the analytical relationships between elastic properties and wave propagation speed.

4. Wave propagation model for orthotropic elastic media

4.1 Generalized case

The model is based on expressions (5) and (6). The solution to Equation (5) actually takes the form of a progressive plane wave, as exhibited in the following expression (Alves et al. 2015; Cuxac 1991):

$$\vec{u}(\vec{OM}, t) = \vec{U} \cdot g(\omega \cdot t - \vec{k} \cdot \vec{OM}) \quad (11)$$

\vec{U} is the maximum displacement vector corrected by function g . \vec{k} designates the wave vector, which is dependent on wave type (compression or shear waves); it is oriented by the unit propagation direction vector \vec{n} , hence:

$$\vec{k} = k_\phi \cdot \vec{n} \quad (12)$$

k_ϕ is defined as the ratio of wave pulsation ω to phase velocity V_ϕ for compression waves ($\phi = p$) and for either horizontal or vertical shear waves ($\phi = S_h$ or $\phi = S_v$, respectively), as defined in the local reference shown in Fig. 8. Its form is given by:

$$k_\phi = \frac{\omega}{V_\phi} \quad (13)$$

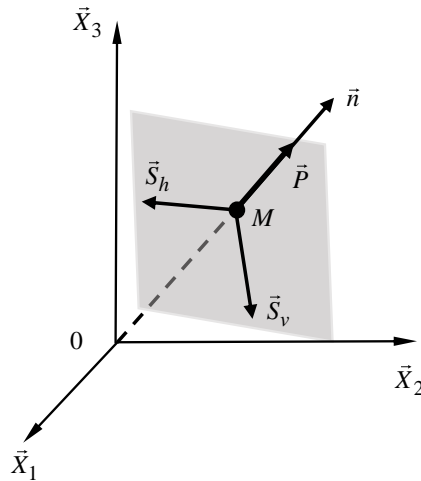


Fig. 8 Local reference

The solution to the dynamic wave propagation equation (5) assumes the typical indicial form below:

$$u_i = U_i \cdot \exp(\omega \cdot t - k_\phi \cdot n_j \cdot x_j) \quad (14)$$

Introducing expression (14) into the left-hand term of (5) yields:

$$\rho \cdot \frac{\partial^2 u_i}{\partial t^2} = \rho \cdot \omega^2 \cdot [U_i \cdot \exp(\omega \cdot t - k_\phi \cdot n_j \cdot x_j)] \quad (15)$$

Similarly, the right-hand term of (5) becomes:

$$\frac{\partial^2 u_l}{\partial x_j \partial x_k} = k_\phi^2 \cdot n_j \cdot n_k \cdot [U_l \cdot \exp(\omega \cdot t - k_\phi \cdot n_j \cdot x_j)] \quad (16)$$

By combining expressions (15) and (16), relation (5) is replaced by:

$$\rho \cdot \omega^2 \cdot U_i = C_{ijkl} \cdot k_\phi^2 \cdot n_j \cdot n_k \cdot U_l \quad (17)$$

Expression (13) enables us to transform equation (17) as follows:

$$\rho \cdot V_\phi^2 \cdot U_i = C_{ijkl} \cdot n_j \cdot n_k \cdot U_l \quad (18)$$

According to Christoffel's notations, expression (18) then becomes:

$$\rho \cdot V_\phi^2 \cdot U_i = \Gamma_{il} \cdot U_l \quad \text{with} \quad \Gamma_{il} = C_{ijkl} \cdot n_j \cdot n_k \quad (19)$$

By developing expression (19), we obtain the following system of equations:

$$\begin{bmatrix} \Gamma_{11} - \rho \cdot V_\phi^2 & \Gamma_{12} & \Gamma_{13} \\ \Gamma_{12} & \Gamma_{22} - \rho \cdot V_\phi^2 & \Gamma_{23} \\ \Gamma_{13} & \Gamma_{23} & \Gamma_{33} - \rho \cdot V_\phi^2 \end{bmatrix} \cdot \begin{pmatrix} U_1 \\ U_2 \\ U_3 \end{pmatrix} = \begin{pmatrix} 0 \\ 0 \\ 0 \end{pmatrix} \quad (20)$$

According to the general case, the solution to the system in (20) is obtained by calculating the eigenvalues of the matrix system. In this case, three values or V_ϕ , corresponding to one compressive and two shear wave velocities, are deduced from solving the characteristic polynomial given by the following expression:

$$\det \begin{bmatrix} \Gamma_{11} - \rho \cdot V_\phi^2 & \Gamma_{12} & \Gamma_{13} \\ \Gamma_{12} & \Gamma_{22} - \rho \cdot V_\phi^2 & \Gamma_{23} \\ \Gamma_{13} & \Gamma_{23} & \Gamma_{33} - \rho \cdot V_\phi^2 \end{bmatrix} = 0 \quad (21)$$

4.2 Adaptation to orthotropic materials

Several researchers have demonstrated the dependence of wave propagation velocity and dynamic modulus of elasticity (in longitudinal, radial and tangential directions of wood (Marra et al. 1966; Dackermann et al. 2016)). At the macroscopic scale, wood is typically considered as an orthotropic material. The mechanical properties of wood differ in the three directions: longitudinal direction (L) parallel to the fibers, radial direction (R) oriented from the bark to the pith, and tangential direction (T) tangent to the growth rings and perpendicular to the grain. These main material axes ($\vec{L}, \vec{R}, \vec{T}$) coincide with the Cartesian coordinate system ($\vec{X}_1, \vec{X}_2, \vec{X}_3$) (Fig. 9).

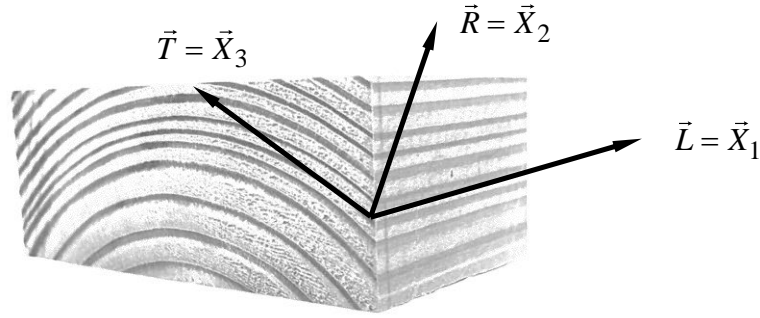


Fig. 9 Orthotropic reference for wood material

For orthotropic materials, linear elastic behavior is usually described by use of the compliance tensor \mathbf{S} , whereby:

$$\mathbf{S} = \mathbf{C}^{-1} \quad (22)$$

Moreover, by considering tensor symmetries, an equation simplification consists of replacing the stress and strain tensors by their equivalent vectors composed of six components. In this case, the Hooke's law equation can be written in the following form:

$$\varepsilon_m = S_{mn} \cdot \sigma_n \text{ or } \{\varepsilon\} = [S] \cdot \{\sigma\} \quad (23)$$

σ_n denotes the stress vector ($\{\sigma\}$) components according to the following correspondence:

$$\sigma_1 = \sigma_{11}, \sigma_2 = \sigma_{22}, \sigma_3 = \sigma_{33}, \sigma_4 = \sigma_{23}, \sigma_5 = \sigma_{13} \text{ and } \sigma_6 = \sigma_{12} \quad (24)$$

Since the thermodynamic balance must be verified, the normal and shear strains ε_m composing the strain vector $\{\varepsilon\}$ are defined below:

$$\varepsilon_1 = \varepsilon_{11}, \varepsilon_2 = \varepsilon_{22}, \varepsilon_3 = \varepsilon_{33}, \varepsilon_4 = 2 \cdot \varepsilon_{23}, \varepsilon_5 = 2 \cdot \varepsilon_{13} \text{ and } \varepsilon_6 = 2 \cdot \varepsilon_{12} \quad (25)$$

S_{mn} are the components of the contracted compliance tensor $[S]$. In the main orthotropic reference, this compliance tensor is defined by:

$$[S] = \begin{bmatrix} \frac{1}{E_L} & -\frac{\nu_{RL}}{E_R} & -\frac{\nu_{TL}}{E_T} & 0 & 0 & 0 \\ -\frac{\nu_{RL}}{E_R} & \frac{1}{E_R} & -\frac{\nu_{TR}}{E_T} & 0 & 0 & 0 \\ -\frac{\nu_{TL}}{E_T} & -\frac{\nu_{TR}}{E_T} & \frac{1}{E_T} & 0 & 0 & 0 \\ 0 & 0 & 0 & \frac{1}{G_{RT}} & 0 & 0 \\ 0 & 0 & 0 & 0 & \frac{1}{G_{LT}} & 0 \\ 0 & 0 & 0 & 0 & 0 & \frac{1}{G_{LR}} \end{bmatrix} \quad (26)$$

where E_α is the Young's modulus corresponding to the α direction. $G_{\alpha\beta}$ and $\nu_{\alpha\beta}$ are the shear modulus and Poisson's ratio corresponding to the $\alpha\beta$ -plane, respectively ($(\alpha, \beta) \in \{L, R, T\}^2$).

According to expression (22), the contracted stiffness tensor $[C]$ can be introduced in accordance with the following form:

$$[C] = [S]^{-1} \text{ and } \sigma_n = C_{mn} \cdot \varepsilon_m \quad (27)$$

4.3 Influence of the fiber angle

This part seeks to integrate a misalignment between the propagation direction given in a global reference $(\vec{X}_1, \vec{X}_2, \vec{X}_3)$ and the principal orthotropic directions $(\vec{L}, \vec{R}, \vec{T})$. This step considers a simple rotation θ around the tangential direction by assigning the unit propagation direction vector \vec{n} along direction \vec{X}_1 (Fig. 10).

In the reference $(\vec{X}_1, \vec{X}_2, \vec{X}_3)$, the stress and strain tensors ($\underline{\underline{\sigma}}'$ and $\underline{\underline{\varepsilon}}'$, respectively) are explained by means of the following transitional functions:

$$\underline{\underline{\sigma}}' = [R_\theta] \cdot \underline{\underline{\sigma}} \cdot [R_\theta]^T \quad \text{and} \quad \underline{\underline{\varepsilon}}' = [R_\theta] \cdot \underline{\underline{\varepsilon}} \cdot [R_\theta]^T \quad (28)$$

$[R_\theta]$ and $[R_\theta]^T$ represent the rotation matrix and its transpose form, in the LR plane, such that:

$$[R_\theta] = \begin{bmatrix} \cos \theta & -\sin \theta & 0 \\ \sin \theta & \cos \theta & 0 \\ 0 & 0 & 1 \end{bmatrix} \quad (29)$$

By adopting the notations in (24) and (25), the expressions in (28) assume the two following forms:

$$\{\sigma\}' = [T_\sigma] \cdot \{\sigma\} \cdot [T_\sigma]^T \quad \text{and} \quad \{\varepsilon\}' = [T_\varepsilon] \cdot \{\varepsilon\} \cdot [T_\varepsilon]^T \quad (30)$$

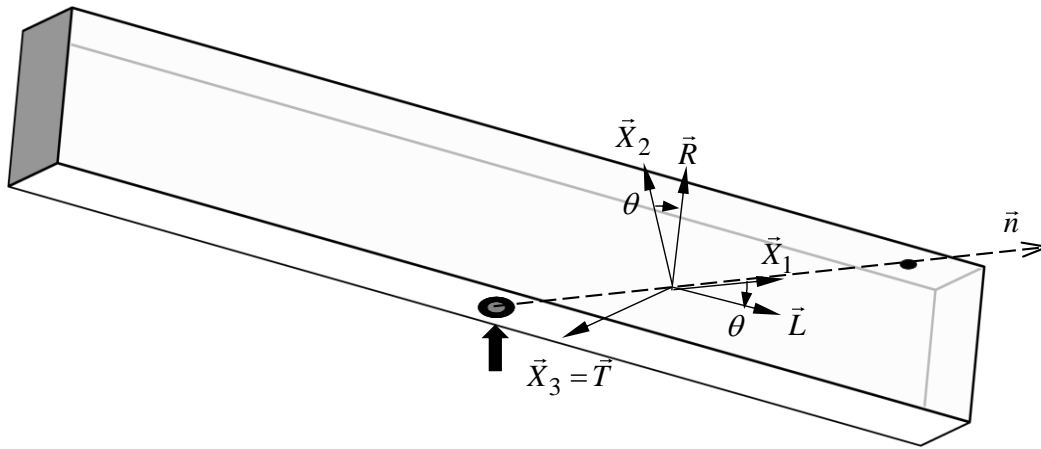


Fig. 10 Local coordinate system positioning

$[T_\sigma]$ and $[T_\varepsilon]$ denote the two contracted rotation matrices, as per their following definitions:

$$[T_\sigma] = \begin{bmatrix} \cos^2 \theta & \sin^2 \theta & 0 & 0 & 0 & -2 \cdot \sin \theta \cdot \cos \theta \\ \sin^2 \theta & \cos^2 \theta & 0 & 0 & 0 & 2 \cdot \sin \theta \cdot \cos \theta \\ 0 & 0 & 1 & 0 & 0 & 0 \\ 0 & 0 & 0 & \cos^2 \theta & \sin^2 \theta & 0 \\ 0 & 0 & 0 & -\sin^2 \theta & \cos^2 \theta & 0 \\ \sin \theta \cdot \cos \theta & -\sin \theta \cdot \cos \theta & 0 & 0 & 0 & \cos^2 \theta \cdot \sin^2 \theta \end{bmatrix} \quad (31)$$

$$[T_\varepsilon] = \begin{bmatrix} \cos^2\theta & \sin^2\theta & 0 & 0 & 0 & -\sin\theta \cdot \cos\theta \\ \sin^2\theta & \cos^2\theta & 0 & 0 & 0 & \sin\theta \cdot \cos\theta \\ 0 & 0 & 1 & 0 & 0 & 0 \\ 0 & 0 & 0 & \cos^2\theta & \sin^2\theta & 0 \\ 0 & 0 & 0 & -\sin^2\theta & \cos^2\theta & 0 \\ 2 \cdot \sin\theta \cdot \cos\theta & -2 \cdot \sin\theta \cdot \cos\theta & 0 & 0 & 0 & \cos^2\theta \cdot \sin^2\theta \end{bmatrix} \quad (32)$$

By introducing the two matrices (31) and (32) into the mechanical behavior (23), it becomes straightforward to define the apparent compliance tensor $[S]'$, i.e.:

$$[S]' = [T_\varepsilon] \cdot [S] \cdot [T_\sigma]^{-1} \quad (33)$$

Similarly, Equation (27) can be rewritten as follows:

$$[C]' = [T_\sigma] \cdot [C] \cdot [T_\eta]^{-1} \quad (34)$$

These relations allow us to take into account the misalignment between the direction of wave propagation and the longitudinal direction.

4.4 Compression wave propagation velocity

Since the present investigations are limited to compression wave propagation, let's now consider an elastic propagation wave along a direction parallel to \vec{X}_1 . Under this condition, the compression wave propagates in the form of a unidirectional wave whose path connects the transmitter to the receiver (Fig. 11).

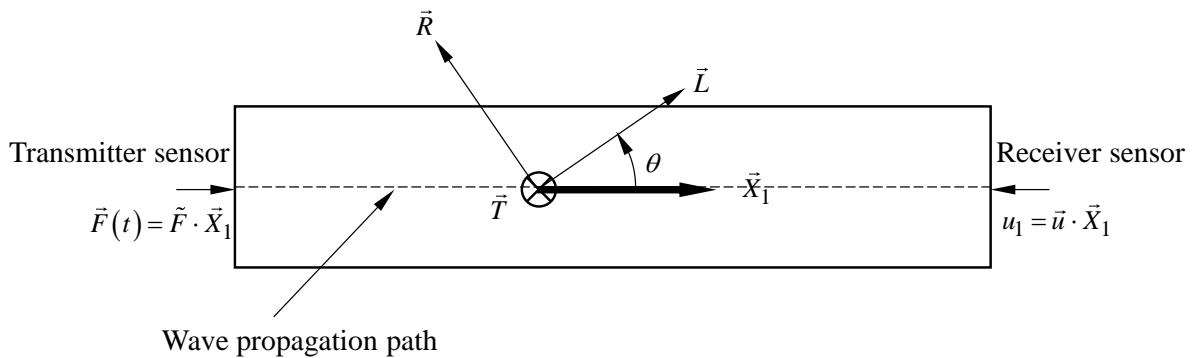


Fig. 11 Compression wave propagation diagram

The transmitter transmits a compression wave by soliciting the sample surface with an impulse force oriented along \vec{X}_1 and distributed evenly over the contact surface s , thus inducing a stress distribution, i.e.:

$$\{\sigma\}^T = \{\sigma_1, 0, 0, 0, 0, 0\}_{(\vec{X}_1, \vec{X}_2, \vec{X}_3)} \text{ with } \sigma_{11} = \frac{\tilde{F}(t)}{s} \quad (35)$$

\tilde{F} denotes the projected force along \vec{X}_1 . In a numerical approach, its form is similar to expression (7).

Given that the receiver sensor is solely sensitive to the compression wave, only the displacement component u_1 along the path propagation is to be considered. Under this condition, only the normal strain component ε_1 can be utilized according to the following expression:

$$\varepsilon_1 = S'_{11} \cdot \sigma_1 \text{ or } \sigma_1 = C'_{11} \cdot \varepsilon_1 \quad (36)$$

With these conditions, the roots of the characteristic Christoffel polynomial, i.e. Equation (21), allow determining the relationship linking compression wave velocity V_p and elastic stiffness C'_{11} , such that:

$$V_p = \sqrt{\frac{C'_{11}}{\rho}} \quad (37)$$

By combining expressions (26), (27) and (34), C'_{11} is defined as follows:

$$C'_{11} = \frac{E_1 \cdot (1 - \nu_{23} \cdot \nu_{32})}{1 - \nu_{12} \cdot \nu_{21} - \nu_{23} \cdot \nu_{32} - \nu_{13} \cdot \nu_{31} - 2 \cdot \nu_{12} \cdot \nu_{23} \cdot \nu_{31}} \quad (38)$$

All elastic orthotropic properties are redefined in the reference $(\vec{X}_1, \vec{X}_2, \vec{X}_3)$ in accordance with the following definitions:

$$E_1 = \frac{1}{\frac{\cos^4 \theta}{E_L} + \frac{\sin^4 \theta}{E_R} + \frac{\cos^2 \theta \cdot \sin^2 \theta}{G_{LR}} - \frac{2 \cdot \nu_{RL} \cdot \cos^2 \theta \cdot \sin^2 \theta}{E_R}} \quad (39)$$

$$E_2 = \frac{1}{\frac{\sin^4 \theta}{E_L} + \frac{\cos^4 \theta}{E_R} + \frac{\cos^2 \theta \cdot \sin^2 \theta}{G_{LR}} - \frac{2 \cdot \nu_{RL} \cdot \cos^2 \theta \cdot \sin^2 \theta}{E_R}} \quad (40)$$

$$E_3 = E_T \quad (41)$$

$$v_{12} = \frac{\frac{v_{RL}}{E_R} - \cos^2 \theta \cdot \sin^2 \theta \cdot \left(\frac{1}{E_L} + \frac{1}{E_R} + \frac{2 \cdot v_{RL}}{E_R} - \frac{1}{G_{LR}} \right)}{\frac{\cos^4 \theta}{E_L} + \frac{\sin^4 \theta}{E_R} + \frac{\cos^2 \theta \cdot \sin^2 \theta}{G_{LR}} - \frac{2 \cdot v_{RL} \cdot \cos^2 \theta \cdot \sin^2 \theta}{E_R}} \quad (42)$$

$$v_{21} = \frac{\frac{v_{RL}}{E_R} - \cos^2 \theta_3 \cdot \sin^2 \theta_3 \cdot \left(\frac{1}{E_L} + \frac{1}{E_R} + \frac{2 \cdot v_{RL}}{E_R} - \frac{1}{G_{LR}} \right)}{\frac{\sin^4 \theta_3}{E_L} + \frac{\cos^4 \theta_3}{E_R} + \frac{\cos^2 \theta_3 \cdot \sin^2 \theta_3}{G_{LR}} - \frac{2 \cdot v_{RL} \cdot \cos^2 \theta_3 \cdot \sin^2 \theta_3}{E_R}} \quad (43)$$

$$v_{13} = \frac{\frac{v_{TL}}{E_T} \cdot \cos^2 \theta + \frac{v_{TR}}{E_T} \cdot \sin^2 \theta}{\frac{\cos^4 \theta}{E_L} + \frac{\sin^4 \theta}{E_R} + \frac{\cos^2 \theta \cdot \sin^2 \theta}{G_{LR}} - \frac{2 \cdot v_{RL} \cdot \cos^2 \theta \cdot \sin^2 \theta}{E_R}} \quad (44)$$

$$v_{31} = v_{TL} \cdot \cos^2 \theta_3 + v_{TR} \cdot \sin^2 \theta_3 \quad (45)$$

$$v_{23} = \frac{\frac{v_{TL}}{E_T} \cdot \sin^2 \theta + \frac{v_{TR}}{E_T} \cdot \cos^2 \theta}{\frac{\sin^4 \theta}{E_L} + \frac{\cos^4 \theta}{E_R} + \frac{\cos^2 \theta \cdot \sin^2 \theta}{G_{LR}} - \frac{2 \cdot v_{RL} \cdot \cos^2 \theta \cdot \sin^2 \theta}{E_R}} \quad (46)$$

$$v_{32} = v_{TL} \cdot \sin^2 \theta_3 + v_{TR} \cdot \cos^2 \theta_3 \quad (47)$$

Thus, measurements of sound speed in each direction (for several angle) allows us to determine the full elastic compliance matrix.

4.5 Validation

This section proposes a numerical validation by comparing finite element results with the analytical model. For this purpose, let's assume the initial homogeneous moisture content state at 11.9%. The elastic properties are posted in table 1. They come from Zhang's work (Zhang, 2021) based on a numerical optimization approach of the three-dimensional elastic properties by minimizing the differences between measured and calculated wave velocities. The calculation of the analytical wave propagation velocity is based on the use of expression (37) considering the set of intermediate calculations grouping equations (38) to (47).

Table 1: Elastic properties at 11.9% of the homogeneous moisture content

ρ	E_L	E_R	E_T	G_{LR}	
503 kg/m ³	16.8 GPa	1.5 GPa	0.88 GPa	1.1 GPa	
ν_{LR}	ν_{RL}	ν_{LT}	ν_{TL}	ν_{RT}	ν_{TR}
0.45	0.04	0.56	0.03	0.68	0.41

The comparison between the analytical model, finite element approach and basic experimental measurements is shown in Fig. 12.

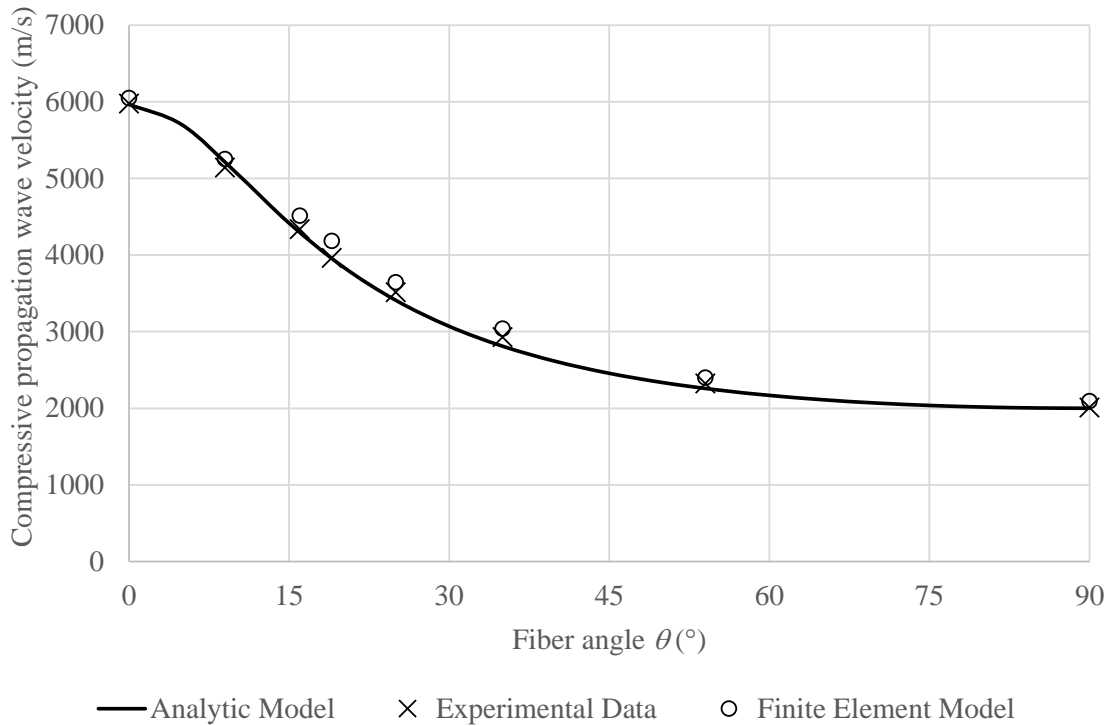


Fig. 12 Evolution in numerical VP vs. the fiber angle

This result highlights a good interpolation of experimental data by the analytical model, with a maximum error less than 4%. The small differences can be interpreted as an imperfect homogeneity of mechanical properties in the beam, as induced by natural dispersion, and an imperfect moisture content stabilization. Moreover, the analytical model cannot be used for a heterogeneous medium, which constitutes the main limitation of this approach.

Regarding the tridimensional finite element model, it reveals slightly higher errors (5%). This finding can be explained by the difficulty involved in calculating the time-of-flight induced by echo phenomena near the receiver sensor at the surface caused by the absence of absorbing boundaries in the case of an

orthotropic medium. Because the dynamic finite element calculation is performed in a three-dimensional configuration, echo effects are accentuated. Moreover, the numerical calculation is sensitive to both the element discretization size and time increment. Finally, this 5% error confirms the decision to conduct the analytical approach under a two-dimensional configuration. On the other hand, the finite element model makes it possible to consider a heterogeneity of the elastic properties, a feature the analytical model does not allow. However, the resolution times (three hours of calculation with an i7 CPU workstation and a Linux operating system) are too long to consider the approach as presently operational, especially for three-dimensional problems and, in previous works, to undertake inverse analysis algorithms to determine, for example, a mechanical or moisture property field. The next section of this paper will propose a hybrid approach coupling both the analytical and finite element approaches.

5. Hybrid approach

This hybrid method is based on combining the analytical model and the finite element implementation. This technique must allow for high-speed resolution, specific to the analytical model, while integrating material heterogeneity into the finite element resolution. Because material heterogeneity can be caused by a moisture content gradient, let's first focus on a mass transfer calculation in accordance with 50 rewetting days induced by the irrigation principle. The finite element support will be used only to determine the water status by solving a mass transfer problem. The calculation of wave propagation velocities will be done analytically. It is in this spirit that the computation time will be greatly reduced compared to a classical dynamic problem (less than ten seconds in comparison with 3 computation hours with a usual finite element approach). Since the ultrasonic velocity measurements are performed in a median plane of the beam, let us consider a two-dimensional configuration of the heat transfer process. Moreover, since the irrigation is done through the extrados of the beam, we can consider, as shown in Figure 3, a mostly vertical water flow adapted with boundary conditions mentioned in Fig. 13. To simplify the understanding of this approach, a two-dimensional problem is introduced in the LR plane.

5.1 Moisture content gradients

The mass transfer algorithm here relies on an algorithm developed in the Manfoumbi Works (Manfoumbi et al., 2014). It is based on a second Fick's law approach and a specific sorption isotherm

model derived by Merakeb et al. (2009) and enhanced by Varnier's characterizations (Varnier et al., 2018). The moisture content evolution w is given by the following differential equation:

$$\frac{\partial w}{\partial t} = \text{div}\left(\underline{\underline{D}}_w(w) \cdot \overrightarrow{\text{grad}}(w)\right) \quad (48)$$

$\underline{\underline{D}}_w(w)$ is a second-order moisture content-dependent diffusion tensor. In the orthotropic reference, this tensor is diagonal with three coordinates, i.e.:

$$D_w^\alpha(w) = D_o^\alpha \cdot \exp(k^\alpha \cdot w), \quad \alpha \in (L, R) \quad (49)$$

where D_o^α denotes three anhydrous diffusion coefficients for each orthotropic direction. k^α is a nonlinear coefficient. For Douglas fir, Manfoumbi et al. (2014) has characterized the values listed below in Table 2.

Table 2: Diffusion properties for Douglas fir

$D_o^L = 1,04 \cdot 10^{-9} m \cdot s^{-1}$	$D_o^R = 2,48 \cdot 10^{-10} m \cdot s^{-1}$
$k^L = 0,0$	$k^R = 0,25$

The boundary conditions necessitate the introduction of a second Fick's law to consider surface exchanges, such as convective effects through a surface exchange coefficient S . According to a continuous hydric flux, Equation (48) can be generalized as follows:

$$\text{div}\left(\underline{\underline{D}}_w(w) \cdot \overrightarrow{\text{grad}}(w)\right) = S \cdot (w_{surf} - w_{bal}) \quad (50)$$

where w_{surf} is the moisture content in the sample periphery. w_{bal} is the equilibrium moisture content between the climatic environment, as defined by its relative humidity RH , and the surface wood fibers. It is defined with sorption isotherm sources defined by Merakeb et al. (2009) and Varnier's characterizations (Varnier et al. 2020). The relationship between w_{bal} and RH is given by:

$$\ln\left(\frac{w_{bal}}{w_s}\right) = \phi \cdot \ln(RH) \cdot \exp(a \cdot RH) \quad (51)$$

w_s is the saturated moisture content defined at 100% RH, ϕ and a . For adsorption cases, all exchange parameters are given in Table 3.

Table 3: Exchange parameters

$S = 10^{-5} m^2 \cdot s^{-1}$	$w_s = 30\%$	$\phi = 0.82$	$a = 1.435$
--------------------------------	--------------	---------------	-------------

w_{bal} is characterized by considering the moisture exposure of the given element. In the case of 50 rewetting days induced by the irrigation principle, Fig. 13 shows the distribution of w_{bal} in the beam periphery.

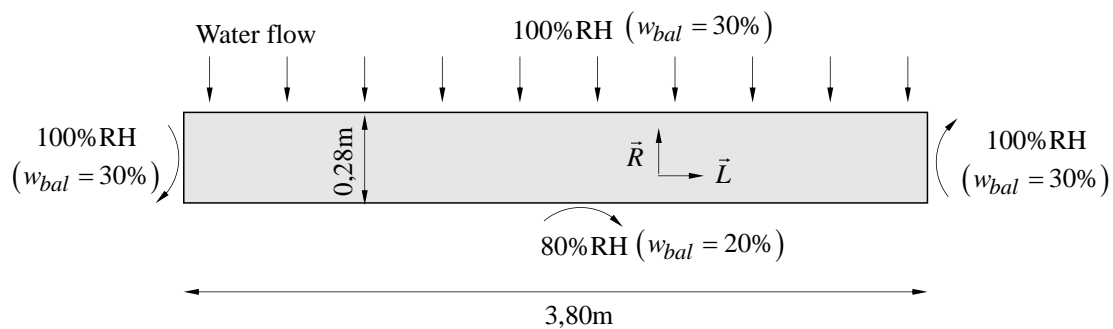


Fig. 13 Convective conditions in the moisture uptake

Although the beam is in direct contact with the irrigation water, it is assumed that the entire element remains within the hygroscopic domain. The 2D mesh is composed of 10,640 regular isoperimetric elements. The time increment is set at 1 hour. After a simulation corresponding to 50 irrigation days, the moisture content map is corrected to obtain an average value of 17.6%, which is in agreement with experimental measurements (Fig. 14).

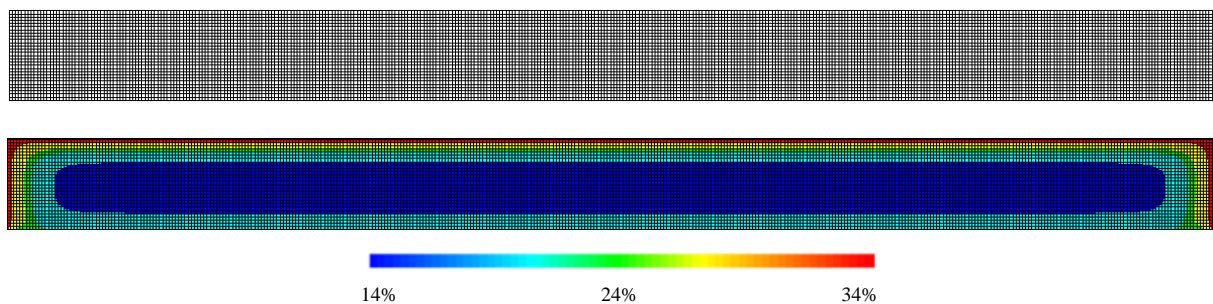


Fig. 14 Finite element mesh and moisture content map after 50 days of irrigation

5.2 Distribution of mechanical properties

Since mechanical properties are dependent on moisture content w , it is proposed to build the mechanical property map according to the following corrections. First, the material density $\rho(w)$ is calculated with its anhydrous value ρ_o and the volume shrinkage-swelling coefficient α_v , such that:

$$\rho(w) = \rho_o \cdot \frac{1+w}{1+\alpha_v \cdot w} \quad (52)$$

Similarly, the elastic properties are corrected using Guitard's formulae (Guitard and El Amri 1987):

$$E_L(w) = E_L(0.12) \cdot [1 - 1.5 \cdot (w - 0.12)] \quad (53)$$

$$E_R(w) = E_R(0.12) \cdot [1 - 3.0 \cdot (w - 0.12)] \quad (54)$$

$$E_T(w) = E_{RT}(0.12) \cdot [1 - 3.0 \cdot (w - 0.12)] \quad (55)$$

$$G_{LR}(w) = G_{LR}(0.12) \cdot [1 - 2.0 \cdot (w - 0.12)] \quad (56)$$

where $E_L(0.12)$, $E_R(0.12)$, $E_T(0.12)$ and $G_{LR}(0.12)$ are the elastic constants defined at the reference moisture content of 12%. In the present case, the reference elastic properties and anhydrous density are given in Table 4.

Table 4: Elastic reference values at 12%

ρ_o	α_v	$E_L(0.12)$	$E_R(0.12)$	$E_T(0.12)$	$G_{LR}(0.12)$
443 kg/m ³	0,1	17 GPa	1,6 GPa	0,91 GPa	1,1 GPa

Considering the internal moisture field, visualized in Fig. 14, in the expressions (52) to (56), the density and mechanical properties fields as shown in Fig. 15 are obtained.

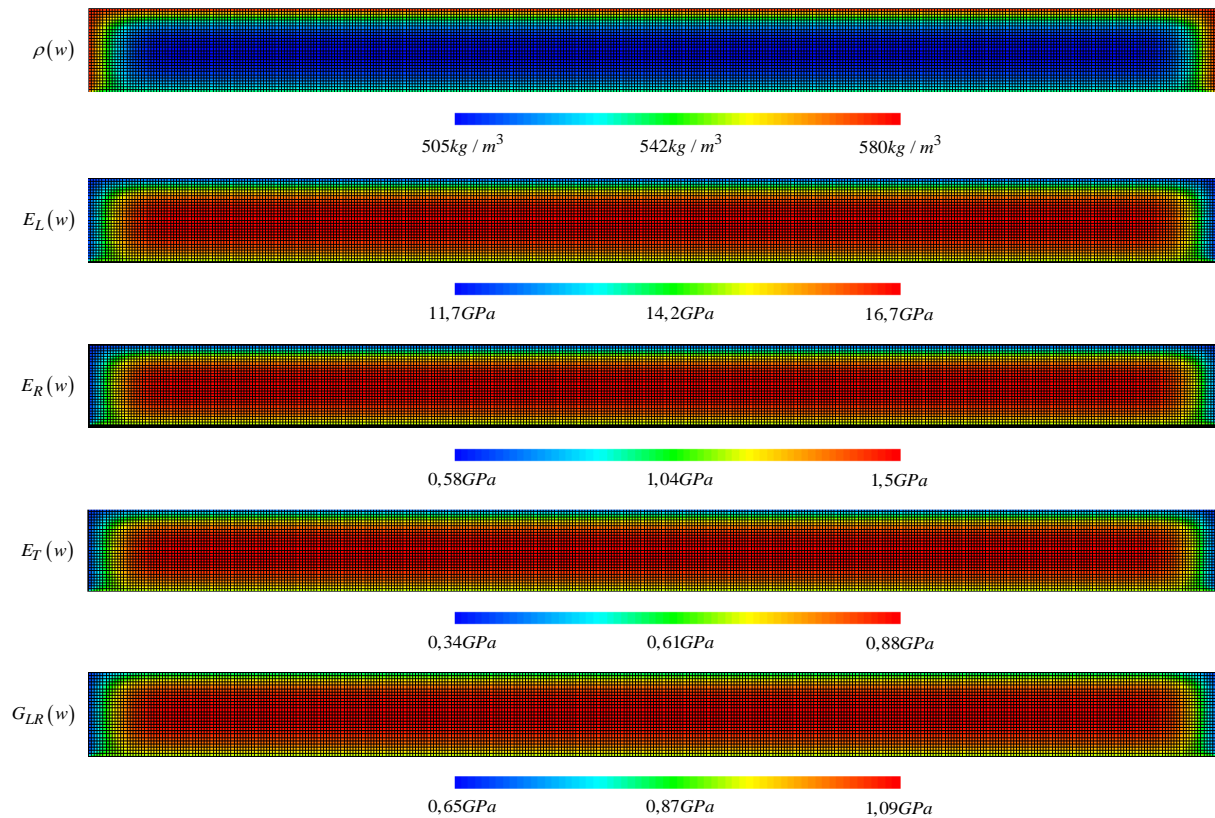


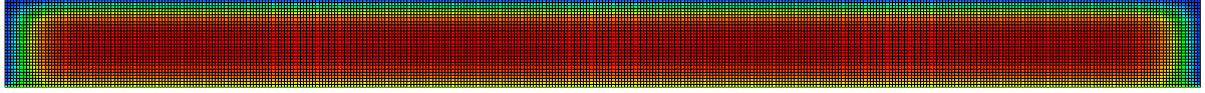
Fig. 15 Density and elastic properties map after 50 days of irrigation

After 50 irrigation days, the simulation indicates a relatively large heterogeneity in density and elastic property distributions.

5.3 Wave propagation velocity distribution

The calculation of wave propagation velocities is divided into three steps. First, by applying Equation (37) and integrating angle corrections (expressions (38) through (47)), in accordance with density and elastic property maps, the finite element computation allows determining wave propagation velocities for all mesh integration points as well as for various angles θ (Fig. 16). Results reveal a velocity heterogeneity induced by the moisture content distribution.

Illustration : Wave propagation velocity fields for $\theta = 0^\circ$



4820 m·s⁻¹  6020 m·s⁻¹

θ	$V_{P\min}$	$V_{P\text{average}}$	$V_{P\max}$
0°	4820 m·s ⁻¹	5734 m·s ⁻¹	6020 m·s ⁻¹
9°	4120 m·s ⁻¹	5050 m·s ⁻¹	5320 m·s ⁻¹
16°	3300 m·s ⁻¹	4190 m·s ⁻¹	4440 m·s ⁻¹
19°	2960 m·s ⁻¹	3820 m·s ⁻¹	3060 m·s ⁻¹
25°	2470 m·s ⁻¹	3290 m·s ⁻¹	3520 m·s ⁻¹
35°	1950 m·s ⁻¹	2715 m·s ⁻¹	2920 m·s ⁻¹
54°	1440 m·s ⁻¹	2165 m·s ⁻¹	2360 m·s ⁻¹
90°	1240 m·s ⁻¹	1930 m·s ⁻¹	2110 m·s ⁻¹

Fig. 16 Mapping of wave propagation velocity vs. θ (illustration for $\theta = 0^\circ$)

The second step consists of defining various path propagation meshes as lines composed of isoperimetric segments following a projection of different wave propagation velocity maps (for different angles) along these lines (Fig. 17).

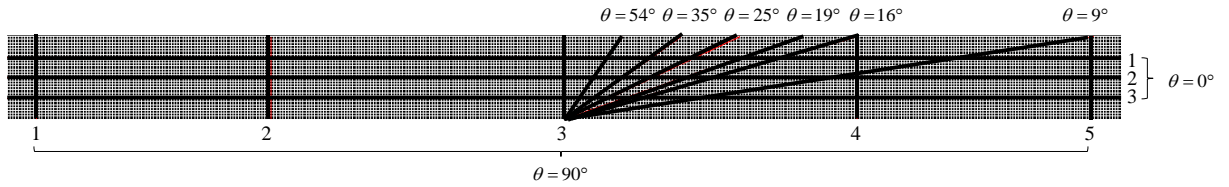


Fig. 17 Different path propagation L_θ for various angles

A final step deals with a curvilinear integration of the wave propagation velocity, for each angle θ , thus allowing for the calculation of average velocity $V_p(L, \theta)$ on each path propagation line, i.e.:

$$V_p(L_\theta, \theta) = \frac{\int_{L_\theta} V_p(s, \theta) ds}{L_\theta} \quad (57)$$

$V_p(s, \theta)$ denotes the curvilinear wave propagation velocity distribution. L_θ is the line propagation length for each angle θ . A comparison of this hybrid model with a classic dynamic resolution and experimental measurements is presented in Fig. 18.

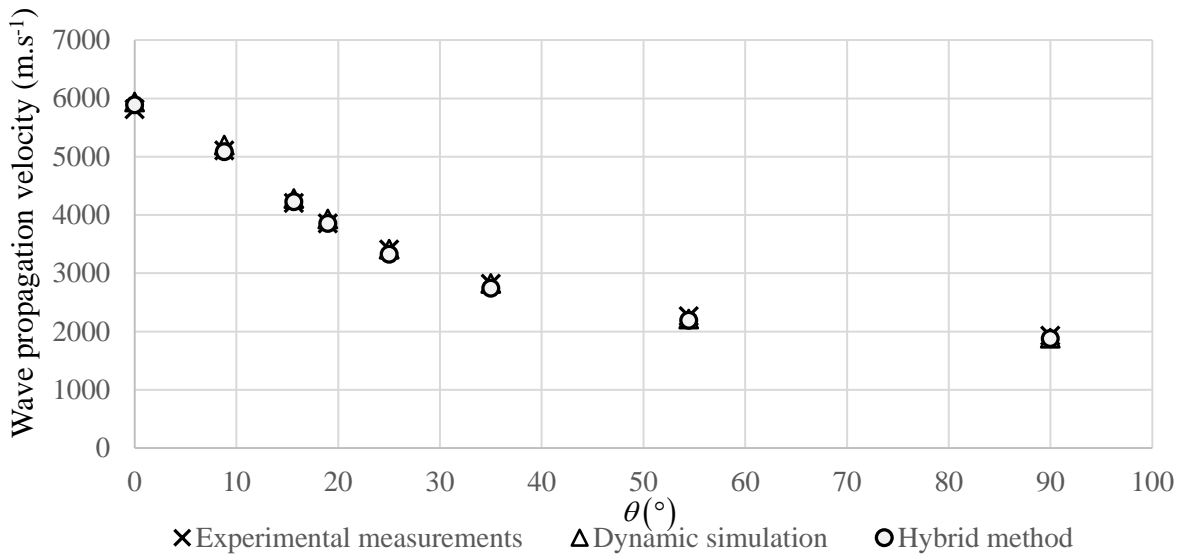


Fig. 18 Modeling and experimental results

A few remarks are necessary at this stage of the study. In comparing the results obtained by the dynamic simulation and hybrid simulation, differences of less than 3% were observed. These errors were common to both methods. First, a dynamic simulation generates echoes at the borders near reception points, which can cause time-of-flight measurement errors. Second, the hybrid method requires projecting the velocity fields onto the wave propagation lines. Even using high-density isoperimetric elements, this projection induces errors in the distribution of velocities on each propagation path, which only increase when these propagation lines are not aligned with the mesh elements. However, while the dynamic simulation requires several hours of computation to obtain all the propagation speeds, the hybrid method makes it possible to obtain this same information in just a few seconds because it is not necessary to solve the finite element problem. The finite element platform is only used, on the one hand, to calculate the elastic property fields and, on the other hand, to carry out the various speed projections on the wave propagation lines.

In contrast, the errors observed between the hybrid method and experimental measurements are mainly explained by the fact that a measurement of the humidity field in the structure is unavailable at this stage of the work. Even though the water field introduced in the hybrid method is a field simulated by using boundary conditions close to reality, it necessarily introduces errors.

6. Conclusion and perspectives

The hybrid model, based on a coupling of the finite element approach and an analytical model, is indeed capable of calculating the wave propagation velocity by considering a moisture content gradient that induces elastic property heterogeneity. Since the time-of-flight has not been calculated, the main difference to a standard dynamic finite element computation is its high-speed resolution. Today, the numerical model is based on a recalculation of the moisture content distribution, which requires a heat and mass transfer resolution. The main differences between experimental measurements and numerical model are focused on this poor moisture content interpolation.

In the near future, this hybrid model should be coupled with another technique to evaluate the moisture content state and its time evolution. Such a model could be based on the results of moisture monitoring on timber structures such as to adjust the mass and heat transfer algorithm to obtain more realistic moisture fields and more realistic elastic property distributions. Another approach could be based on experimental dielectric methods for use in better evaluating and isolating the moisture content distribution in the timber element while remaining somewhat uncoupled from the mechanical property evaluation.

More long-term scientific work will focus on developing an inverse method to identify the best compromise, in terms of water content distribution, between the experimental measurements and this hybrid method by minimizing the value of the residual. For example, Newton-Raphson type incremental minimization algorithms are compatible with the computational speed of the wave propagation velocities calculated using this hybrid method.

7. References

- Alves R.C., Mantilla J.N.R., Bremer C.F., Carrasco E.V.M. (2015), Application of Acoustic Tomography and Ultrasonic Waves to Estimate Stiffness Constants of Muiracatiara Brazilian Wood. *Bioresources* 10/1:1845-1856
- Bucur V. (2006), *The Acoustics of Wood*, CRC Press, ISBN: 978-3-540-30594-1.

Cuxac. P (1991), Propagation et atténuation des ondes ultrasoniques dans des roches fissurées et anisotropes (Propagation and attenuation of ultrasonic waves in cracked and anisotropic rocks), PHD Thesis, National Polytechnic Institute of Lorraine

Dackermann U., Elsener R., Li J., Crews K. (2016), A comparative study of using static and ultrasonic material testing methods to determine the anisotropic material properties of wood, *Construction and Building Materials*, 102-2:963-976

De Oliveira F.G.R., Candian M., Lucchette F.F., Salgon J.L., Sales A. (2005), Moisture content effect on Ultrasonic Velocity in *Goupia Glabra*. *Mater. Res.* 8, 11–14, <https://doi.org/10.1590/S1516-14392005000100004>

Dündar T., Wang X., As N., Avcı E. (2016), Potential of ultrasonic pulse velocity for evaluating the dimensional stability of oak and chestnut wood. *Ultrasonics* 66:86–90, <https://doi.org/10.1016/j.ultras.2015.11.007>

Espinosa L., Brancheriau L., Prieto F., Lasaygues P. (2018), Sensitivity of ultrasonic wave velocity estimation using the christoffel equation for wood non-destructive characterization, *Bioressources*, 13:1, 918-928, <https://doi.org/10.15376/biores.13.1.918-928>

Gonçalves R., Lorensani R.G.M., Negreiros T.O., Bertoldo, C. (2018), Moisture-related adjustment factor to obtain a reference ultrasonic velocity in structural lumber of plantation hardwood. *Wood Mater. Sci. Eng.* 13:254–261, <https://doi.org/10.1080/17480272.2017.1313312>

Guitard D., El Amri F. (1987), Modèles prévisionnels de comportement élastique tridimensionnel pour les bois feuillus et les bois résineux (Predictive models of three-dimensional elastic behavior for hardwoods and softwoods), *Annals of Forest Science*, 44 :335–358. <https://doi.org/10.1051/forest:19870305>

Kabir M.F., Daud W.M., Khalid K., Sidek H.A.A. (1998), Effect of moisture content and grain direction on the dielectric properties of rubber wood at low frequencies. *Holzforschung* 52:546–552. <https://doi.org/10.1515/hfsg.1998.52.5.546>

Kabir M.F. (2001), Prediction of ultrasonic properties from grain angle. *Journal of the institute of wood science*, 15,5:89:235-246. ISSN 0020-3203

Kollmann F.F.P., Kuenzi E.W., Stamm A.J. (2012), *Principles of Wood Science and Technology: II Wood Based Materials*. Springer Science & Business Media, <https://doi.org/10.1007/978-3-642-87931-9>.

Komatitsch D., Barnes C., Tromp J. (2000), Simulation of anisotropic wave propagation based upon a spectral element method, *Geophysics* 65:4, 1251-1260, <https://doi.org/10.1190/1.1444816>

Kurz, J.H., Grosse, C.U., and Reinhardt, H.-W. (2005). Strategies for reliable automatic onset time picking of acoustic emissions and of ultrasound signals in concrete. *Ultrasonics* 43, 538–546. <https://doi.org/10.1016/j.ultras.2004.12.005>

Lasaygues, P., Arciniegas, A., and Brancheriau, L. (2014), Comparaison de méthodes de détection de TOF adaptées à la tomographie ultrasonore des arbres sur pied (Comparison of TOF detection methods adapted to ultrasound tomography of standing trees), 12th French Acoustics Congress, Poitiers, France, ISBN 978-2-919340-02-6.

Manfoumbi N., Nguyen T.A., Angellier N., Dubois F., Ulmet L., Sauvat N. (2014), Experimental and numerical aspects in diffusion process characterization in tropical species. *European Journal of Environmental and Civil Engineering*, 18:9:963-982, <https://doi.org/10.1080/19648189.2014.917993>

Marra G.G., Pellerin R.F., Galligan W.L. (1966), Nondestructive determination of wood strength and elasticity by vibration. *Holz Roh- Werkst.* 24, 460–466, ISSN: 1436-736X, 0018-3768

Masumi H., Masato T., Junji M., Kazuyuki O. (2011), Effect of wood properties on within-tree variation in ultrasonic wave velocity in softwood. *Ultrasonics* 51(3):296-302, <https://doi.org/10.1016/j.ultras.2010.10.001>

Matsunaga W., Mizukami K., Mizutani Y., Todoroki A. (2022), Estimation of the moisture absorption rate of glass fiber reinforced plastic , using electromagnetic induction testing, *Composites Part C: Open Access*, <https://doi.org/10.1016/j.jcomc.2022.100260>

McDonald D., Begel M. Senalik, C.A., Ross R. (2014), Creep behavior of structural insulated panels (SIPs): results from a pilot study. USDA For. Serv. For. Prod. Lab. Res. Note FPL-RN-0332, 2014 16 P 332, 1–16.

Merakeb S., Dubois F., Petit C. (2009), Modeling of the sorption hysteresis for wood. *Wood Sci Technol*, 43:7-8, 575-589, <https://doi.org/10.1007/s00226-009-0249-2>

Nguyen T.A., Angellier N., Caré S., Ulmet L., Dubois F. (2017), Numerical and experimental approaches to characterize the mass transfer process in wood elements, *Wood Sci Technol* 51(4):811-830, <https://doi.org/10.1007/s00226-017-0898-5>

Norimoto M., Yamada T. (1970), The dielectric properties of wood IV: On dielectric dispersions of oven-dried wood. *bulletin of the Wood Research Institute Kyoto University* (1970), 50: 36-49

Orta A. H., Vandendriessche J., Kersemans M., Paepegem W. V., Roozen N. B., Abeele K. V. D. (2021), Modeling lamb wave propagation in visco-elastic composite plates using a fifth-order plate theory, *Ultrasonics*, 116, <https://doi.org/10.1016/j.ultras.2021.106482>

Pradhan T. (2014), Finite Element Modeling of Impact-Generated stress wave propagation in concrete plates for non-destructive evaluation. PHD Thesis, Lehigh University.

Rosenkrantz E., Bottero A., Komatitsch D., Monteiller V. (2019), A flexible numerical approach for non-destructive ultrasonic testing based on a time-domain spectral-element method: Ultrasonic modeling of Lamb waves in immersed defective structures and of bulk waves in damaged anisotropic materials, *NDT & E International*, 101, 72-86, <https://doi.org/10.1016/j.ndteint.2018.10.002>

Ross R.J. (1994), Nondestructive Testing for Assessing Wood Members in Structures: A Review, General technical report FPL ; GTR-70, Forest Products Laboratory, <https://doi.org/10.2737/FPL-GTR-70>.

Royer D., Dieulesaint E., De Gennes P.G. (1996), *Ondes élastiques dans les solides - Tome 1 : Propagation libre et guidée (Elastic waves in solids – Vol. 1: Free and guided propagation)*, Masson Edition, ISBN 9782225854224 et 222585422X.

Sakai H., Minamisawa A., Takagi K. (1990), Effect of moisture content on ultrasonic velocity and attenuation in woods. *Ultrasonics* 28, 383–385.

Seron F.J., Sanz F.J., Kindelan M., Badal J.I. (1990), Finite-Element Method for Elastic Wave Propagation, *Communications in Applied Numerical Methods*, 359-368, <https://doi.org/10.1002/cnm.1630060505>

Silva C., Branco J., Mehdipour Z., Xavier J., Lourenço P. (2022), Experimental Stress Analysis of Cross-Laminated Timber Elements under Cyclic Moisture, *Journal of Materials in Civil Engineering*, 34:8, [https://doi.org/10.1061/\(ASCE\)MT.1943-5533.0004336](https://doi.org/10.1061/(ASCE)MT.1943-5533.0004336)

Sridhar R., Chakraborty A., Gopalakrishnan S. (2006), Wave propagation analysis in anisotropic and inhomogeneous uncracked and cracked structures using pseudospectral finite element method, *International Journal of Solids and Structures*, 43:16, 4997-5031, <https://doi.org/10.1016/j.ijsolstr.2005.10.005>

Torgovnikov G.I. (1993), *Dielectric Properties of Wood and Wood-Based Materials*, Springer Berlin Heidelberg, ISBN: 978-3-642-77455-3.

Varnier M., Sauvat N., Montero C., Dubois F., Gril J. (2018), Adaptation of Eurocode 5 standard to French hardwoods – Proposal of new hygroscopic equilibrium charts, *Proc. Meeting 51 INTER*, Tallin.

Varnier M., Sauvat N., Ulmet L., Montero C., Dubois F., Gril J. (2020), Influence of temperature in a mass transfer simulation: application to wood, *Wood Sci Technol* 54(4):943-962, <https://doi.org/10.1007/s00226-020-01197-y>

Vössing K.J., Niederleithinger E., (2018), Nondestructive assessment and imaging methods for internal inspection of timber. A review, *Holzforschung*, 72:6, 467-476, <https://doi.org/10.1515/hf-2017-0122>

Wang X. (2008), Effects of Size and Moisture on Stress Wave E-rating of Structural Lumber. 10th world conference on timber engineering : Miyazaki, Japan.

Zhang, H. (2003), Automatic P-Wave Arrival Detection and Picking with Multiscale Wavelet Analysis for Single-Component Recordings. *Bull. Seismol. Soc. Am.* 93, 1904–1912, <https://doi.org/10.1785/0120020241>

Zhang X., Shao S., Shao S. (2021), A Recursive Legendre Polynomial Analytical Integral Method for the Fast and Efficient Modelling Guided Wave Propagation in Rectangular Section Bars of Orthotropic Materials, *International Journal of Acoustics and Vibrations*, 26:3, 221-230, <https://doi.org/10.20855/ijav.2021.26.31772>

Zhang X. (2021), Surveillance et Auscultation des Ouvrages en bois par Identification des Champs Hydrique et Mécanique : Couplage des Méthodes Acoustiques et Electromagnétiques (Monitoring and Auscultation of Timber Structures by Identification of Hydric and Mechanical Fields: Coupling of Acoustic and Electromagnetic Methods), PHD thesis, Limoges University

Zisi A., Dix J.K. (2017), Simulating mass loss of decaying waterlogged wood: A technique for studying ultrasound propagation velocity in waterlogged archaeological wood, *Journal of Cultural Heritage*, 33: 39–47, <https://doi.org/10.1016/j.culher.2018.02.016>